



# Flexible, controllable, and high-strength near-infrared reflective $\text{Y}_2\text{O}_3$ nanofiber membrane by electrospinning a polyacetylacetone-yttrium precursor

Yongshuai Xie<sup>a</sup>, Lin Wang<sup>a</sup>, Benxue Liu<sup>b</sup>, Luyi Zhu<sup>a,\*</sup>, Shuying Shi<sup>a</sup>, Xinqiang Wang<sup>a</sup>

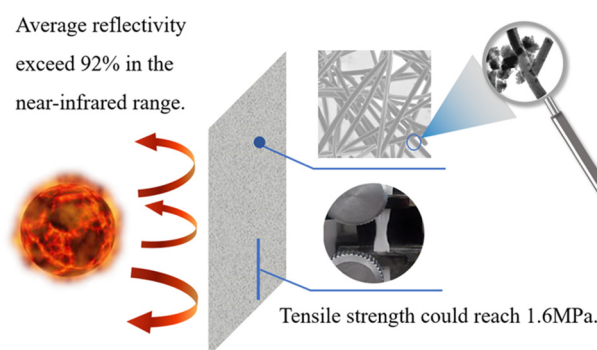
<sup>a</sup> State Key Laboratory of Crystal Materials and Institute of Crystal Materials, Shandong University, Jinan 25010, PR China

<sup>b</sup> Advanced Materials Institute, Shandong Provincial Key Laboratory for Special Silicone-Containing Materials, Qilu University of Technology (Shandong Academy of Science), Jinan 250014, PR China

## HIGHLIGHTS

- Polyacetylacetone-yttrium, a precursor of 42%  $\text{Y}_2\text{O}_3$  content for preparing  $\text{Y}_2\text{O}_3$  fiber membrane, has been synthesized.
- Tensile strength of the flexible, high crystalline cubic  $\text{Y}_2\text{O}_3$  nanofiber membrane could reach 1.6 MPa.
- The average reflectivity of  $\text{Y}_2\text{O}_3$  nanofiber membrane exceeded 92% in the near-infrared range.
- At 1500 °C, the  $\text{Y}_2\text{O}_3$  nanofiber membrane has a certain shielding effect on the near-infrared radiation.

## GRAPHICAL ABSTRACT



## ARTICLE INFO

### Article history:

Received 10 August 2018

Received in revised form 8 October 2018

Accepted 9 October 2018

Available online 11 October 2018

### Keywords:

High near-infrared (NIR) reflectivity

$\text{Y}_2\text{O}_3$

Nanofiber membrane

Electrospinning

## ABSTRACT

High-quality reflective screens constitute an important part of multi-layer insulation materials. However, the metal foils currently used as thermal reflective screens are easily oxidized in an oxidizing environment. Nano-scale yttrium oxide exhibits high reflectivity in the near-infrared (NIR) region, as well as excellent stability in an oxidizing environment. The material also shows potential for application as a high-temperature reflective screen. A high near-infrared reflective  $\text{Y}_2\text{O}_3$  nanofiber membrane was successfully prepared by electrospinning a synthetic polyacetylacetone-yttrium (PAY) precursor into precursor fibers, followed by heat treatment. The new polyorganometallic precursor PAY with 42%  $\text{Y}_2\text{O}_3$  content was synthesized by adjusting the ratio of acetylacetone to  $\text{YCl}_3 \cdot 6\text{H}_2\text{O}$ . The crystallization, microstructure and NIR reflectivity of the  $\text{Y}_2\text{O}_3$  nanofiber membrane were analyzed. The tensile strength of the  $\text{Y}_2\text{O}_3$  nanofiber membrane was evaluated. The strength of the  $\text{Y}_2\text{O}_3$  nanofiber membrane with good flexibility, prefect morphology and high crystallinity could reach 1.6 MPa, and its NIR reflectivity could reach 95%. High-temperature heat-reflective testing shows that the  $\text{Y}_2\text{O}_3$  nanofiber membrane exerts a reflective effect on thermal radiation at 1500 °C. It could be continuously used as a reflective screen for high-temperature insulation materials in a high-temperature oxidizing environment.

© 2018 Published by Elsevier Ltd. This is an open access article under the CC BY-NC-ND license (<http://creativecommons.org/licenses/by-nc-nd/4.0/>).

\* Corresponding author.

E-mail address: [zhulyi@sdu.edu.cn](mailto:zhulyi@sdu.edu.cn) (L. Zhu).

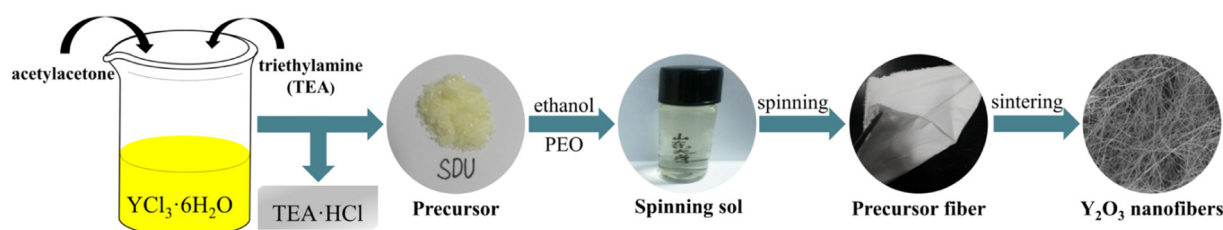


Fig. 1. Preparation process of  $\text{Y}_2\text{O}_3$  nanofibers.

## 1. Introduction

The development of high-temperature thermal insulation materials is significant in defense, aerospace, military, industrial and other fields. Most traditional thermal barrier insulation materials exhibit good permeability to infrared radiation. Heat transfer primarily arises from the presence of a temperature gradient. Radiative heat transfer is attributed to the difference in temperature between cold and hot surfaces, which exceeds 100 °C. Heat transfer basically occurs in three ways: heat radiation, heat conduction, and thermal convection. With respect to heat transfer, thermal insulation materials could be divided into two categories: (i) thermal barrier insulation materials which can reduce thermal conduction and thermal convection, and (ii) heat-reflective materials, which can reflect thermal radiation. According to Boltzmann's law, the rate of infrared radiation increases with the fourth power of temperature [1]. With an increase in temperature, the thermal conductivity of most heat insulation materials increases faster. The distinct thermal radiation reflector of multi-layer thermal insulation materials can effectively inhibit heat radiation transfer by reflection [2]. Hence the development trend of insulation materials toward multilayer insulation materials. Heat-reflective insulation materials, such as  $\text{TiO}_2$  and  $\text{SiO}_2$ , are typically used to reflect sunlight [3,4]. At high temperatures, the materials used as thermal radiation reflectors in multilayer insulation materials include gold foil, copper foil, aluminum foil, nickel foil, molybdenum foil, and stainless steel foil [5–7]. These metal foils are easily oxidized in an oxidizing environment, thereby losing the effect of reflection and heat insulation.

Yttrium oxide ( $\text{Y}_2\text{O}_3$ ) is not only an important rare-earth metal oxide but an excellent ceramic material as well. Owing to its high melting point (2410 °C), high-temperature stability, heat and corrosion

resistance, high dielectric constant, low photon energy, and stability in reducing media [8–11], the material is often used in the production of lasers, magnets, phosphors, and superconductors [8,12–17]. Moreover, nanoscale  $\text{Y}_2\text{O}_3$  exhibits high reflectivity in the NIR region [18], rendering it useful as a NIR-reflective material to overcome of metal foil failure in high temperature oxidation environment. However, no studies have been reported on the use of  $\text{Y}_2\text{O}_3$  as a thermal radiation reflector in multilayer heat insulation materials in a high-temperature oxidizing environment.

Methods for the preparation of nanometer  $\text{Y}_2\text{O}_3$  mainly include vapor deposition, sol-gel, precipitation, and hydrothermal methods [19–22]. Among these techniques, vapor deposition, precipitation and hydrothermal methods are primarily used to prepare nanopowders, nanowires, and other structures with a relatively low aspect ratio [20–23]. The sol-gel method combined with electrospinning can be employed to prepare nanofibers with a high aspect ratio. Researchers have successfully prepared many types of nanofibers using this method and applied them to different fields. Such as silica-filled PVDF fibers used in heat insulation and flame retardant applications [24], and metal doped crosslinked polyacrylonitrile nanofibers for electromagnetic shielding [25]. Thus far, in the only study on  $\text{Y}_2\text{O}_3$  nanofibers, a spinning solution was produced by dissolving yttrium salt into a solution containing numerous organic polymers [26–29]. The precursors exhibited a rather high organic content. Large mass loss of fiber during heat treatment leads to high fiber porosity and low strength. However, studies on  $\text{Y}_2\text{O}_3$  nanofiber have focused on luminescence. No studies have thus far been reported on the NIR-reflective properties of  $\text{Y}_2\text{O}_3$  nanofibers and  $\text{Y}_2\text{O}_3$  nanofiber membranes.

In this study, polyacetylacetone-yttrium (PAY), which is a precursor with high yttria content, was successfully synthesized by adjusting the ratio of acetylacetone to  $\text{YCl}_3 \cdot 6\text{H}_2\text{O}$ . The flexible  $\text{Y}_2\text{O}_3$  nanofiber membrane was simultaneously prepared using PAY. The crystallization and microstructure of  $\text{Y}_2\text{O}_3$  nanofibers were examined. The mechanical properties of the  $\text{Y}_2\text{O}_3$  nanofiber membrane were also analyzed. Lastly, the NIR reflectivity and high-temperature heat reflectivity of the  $\text{Y}_2\text{O}_3$  nanofiber membrane were characterized and discussed. The as-obtained flexible  $\text{Y}_2\text{O}_3$  nanofiber membrane showed high NIR reflectivity.

## 2. Experimental section

### 2.1. Materials

Yttrium chloride hexahydrate ( $\text{YCl}_3 \cdot 6\text{H}_2\text{O}$ , ≥99.0%, Qingda), acetylacetone ( $\text{CH}_3\text{C}(\text{O})\text{CH}_2\text{C}(\text{O})\text{CH}_3$ , AR, Damao), triethylamine ( $\text{N}(\text{CH}_2\text{CH}_3)_3$ , ≥99.5%, Fuyu), acetone ( $\text{CH}_3\text{COCH}_3$ , AR, Fuyu), absolute methanol ( $\text{CH}_3\text{OH}$ , 99.5%, Fuyu), absolute ethanol ( $\text{CH}_3\text{CH}_2\text{OH}$ , 99.5%, Fuyu), and polyethylene oxide (PEO, Mw~1000,000, Aladdin) were used as starting materials in this study. All chemicals were used as starting materials without further purification.

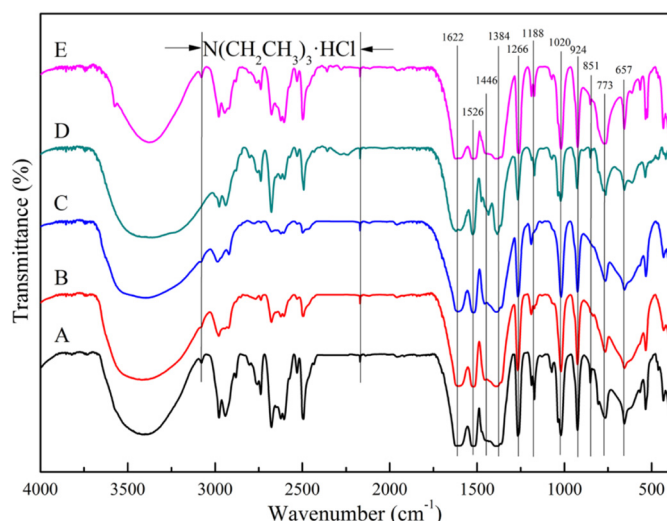


Fig. 2. FT-IR spectra of precursor A to E.

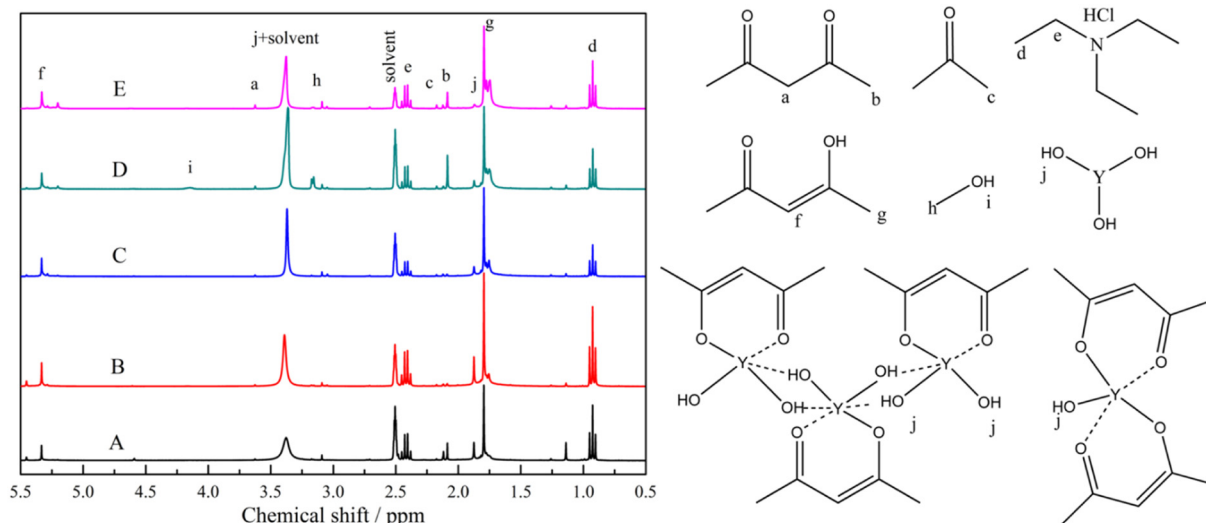


Fig. 3.  $^1\text{H}$  NMR spectra of precursor A to E and attribution of each peak.

## 2.2. Preparation of yttrium oxide nanofibers

The method for the preparation of  $\text{Y}_2\text{O}_3$  nanofibers is illustrated in Fig. 1. The process includes four steps: synthesis of precursors, preparation of the spinning solution, electrospinning of precursor nanofibers, and heat treatment. Different amounts of acetylacetone (16.5, 26.4, 33, 39.6, and 49.5 g) were added into the yttrium chloride solution (consisting of 100 g  $\text{YCl}_3 \cdot 6\text{H}_2\text{O}$  and 320 g methanol) and correspondingly marked as A, B, C, D, and E. After stirring for 30 min, the solution was added with 101 g triethylamine. Solutions A, B and C were clarified, whereas D and E were precipitated (Fig. S1). After the precipitate was filtered, the filter liquor was placed in a round-bottom flask and then dried. Subsequently, 500 mL acetone was added into the flask to soak the dried product. After letting the solution stand for 24 h at room temperature, insoluble triethylamine hydrochloride was filtered from the solution. The filtrate was rotary-evaporated to dryness to synthesize the precursors from A to E. The 6 g precursor and 0.06 g PEO were dissolved in 20 g ethanol, with stirring, to obtain a spinning solution. To homogenize the spinning solution, the solution was continuously stirred for 2 h to complete clarification. Precursor nanofiber membranes were obtained by electrospinning with the following parameters: advancing speed of the syringe pump, 0.8 mL/h; distance between the needle and the receiving plate, 20 cm; and spinning voltage, 11 kV. Precursor nanofiber membranes were heated under air at a rate of  $1^\circ\text{C}/\text{min}$  to a corresponding temperature and then held for 2 h to form  $\text{Y}_2\text{O}_3$  nanofiber membranes.

## 2.3. Characterization

The Fourier transform infrared (FT-IR) spectra of the precursor and preheated fibers were recorded on a Bruker ALPHA FT-IR spectrometer

in the  $4000\text{--}400\text{ cm}^{-1}$  region. The nanofibers were ground into powders and measured using the KBr pellet method.  $^1\text{H}$  nuclear magnetic resonance ( $^1\text{H}$  NMR) spectroscopy was conducted using a Bruker Advance-600 Fourier transform NMR spectrometer with  $\text{DMSO-}d_6$  as the solvent. Thermogravimetric (TG) analysis was conducted using a Perkin Elmer Diamond thermal analyzer. Data were collected up to  $800^\circ\text{C}$  with increments of  $5^\circ\text{C}/\text{min}$  in air. The Elemental vario EL cube element analyzer was used to analyze the contents of C, H and N in the sample. The particle size distribution of the sample in ethanol was obtained by dynamic light scattering (DLS) using Malvern Nano ZS. X-ray diffraction (XRD) patterns for the samples were collected using a Bruker AXSD8 Advance X-ray diffractometer with  $\text{Cu-}K\alpha$  radiation ( $\lambda = 0.1540598\text{ nm}$ ) using a graphite monochromator in the  $2\theta$  range of  $10\text{--}80^\circ$  with a step size of  $0.02^\circ$ . Jade 6.0 was used to index the diffraction patterns. The grain size and crystallinity were also fitted using Jade 6.0. The size and morphology of the materials were analyzed by scanning electron microscopy (SEM) using a Hitachi S-4800 microscope and high-resolution transmission electron microscopy (HRTEM) using a JEOL-2100F microscope. Mechanical properties were analyzed using an LLY-06 electronic fiber strength tester. Diffuse reflectance spectra were measured using a Hitachi U-4150 UV-VIS-NIR spectrometer with

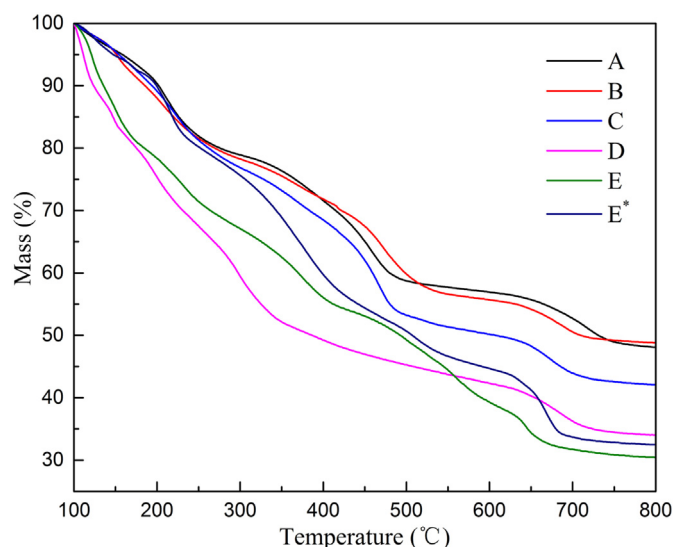


Fig. 4. TG curves of precursor A to E and precipitation of ratio E ( $\text{E}^*$ ).

**Table 1**  
Integral area of partial chemical shift peaks and their relationship.

Chemical shift	Group	A	B	C	D	E
0.90	d	4.10	3.08	1.47	1.66	2.50
2.42	e	2.88	2.15	0.95	1.13	1.72
5.35	f	1	1	1	1	1
1.8	g	5.78	5.83	6.18	5.93	6.21
1.88	j	2.70	2.33	1.79	1.35	0.78
d/e		1.42	1.43	1.55	1.47	1.45
g/f		5.78	5.83	6.18	5.93	6.21
j/f		2.70	2.33	1.79	1.35	0.78



**Table 2**  
Spinning performance of precursors.

No.	Acetylacetone/ $\text{YCl}_3 \cdot 6\text{H}_2\text{O}$	Stability of spinning sol	Fiber length	Spinnability
A	0.5	Poor	2–3 cm	Good
B	0.8	Good	5–7 cm	Better
C	1.0	Best	>10 cm	Best

an integrating sphere accessory. Optical photos were taken with a Huawei mobile phone.

### 3. Results and discussion

#### 3.1. Natural properties and choice of precursor

The FT-IR spectra of precursor A to E are presented in Fig. 2. The peaks at 1622, 1528, 1446, 1384, 1266, and 1188  $\text{cm}^{-1}$  represent the characteristic vibration of acetylacetonate metal complex [30],

indicating the coordination between acetylacetonate and Y ion. In addition, the peaks at 1020, 924, 851 and 773  $\text{cm}^{-1}$  are attributed to  $\text{CH}_3$  rock, C—C symmetric stretching vibration ( $\nu_s$ ), symmetric deformation vibration ( $\nu_s$ , def) of COO, and out-of-plane rocking vibration ( $\omega$ ) of C—H of acetylacetonate confirming the presence of acetylacetonate in PAY [31]. The addition of triethylamine resulted in an alkaline reactant solution, which lead to hydrolysis of Y ions. The peak at 657  $\text{cm}^{-1}$  was attributed to Y-OH vibration [32]. The peaks in samples A, B, and C showed broadening, indicating Y-OH interaction. Sharp peaks at 657  $\text{cm}^{-1}$  were observed in samples D and E, suggesting the weakness or absence of the interaction. The peaks at 3100–2200  $\text{cm}^{-1}$  mainly originated from the characteristic vibration of retained triethylamine hydrochloride attributed to inefficient filtration [33]. Fig. 2 shows that the triethylamine hydrochloride content in the samples first decreases and then increases with increasing molar ratio of Y ion to acetylacetonate. When the molar ratio of Y ion to acetylacetonate is 1:1, the triethylamine hydrochloride content was minimal. Solutions A and B showed high Y (OH)<sub>3</sub> content, and easily formed large particles. The results of DLS analysis (Fig. S2) clearly showed that the particles of samples A and B in

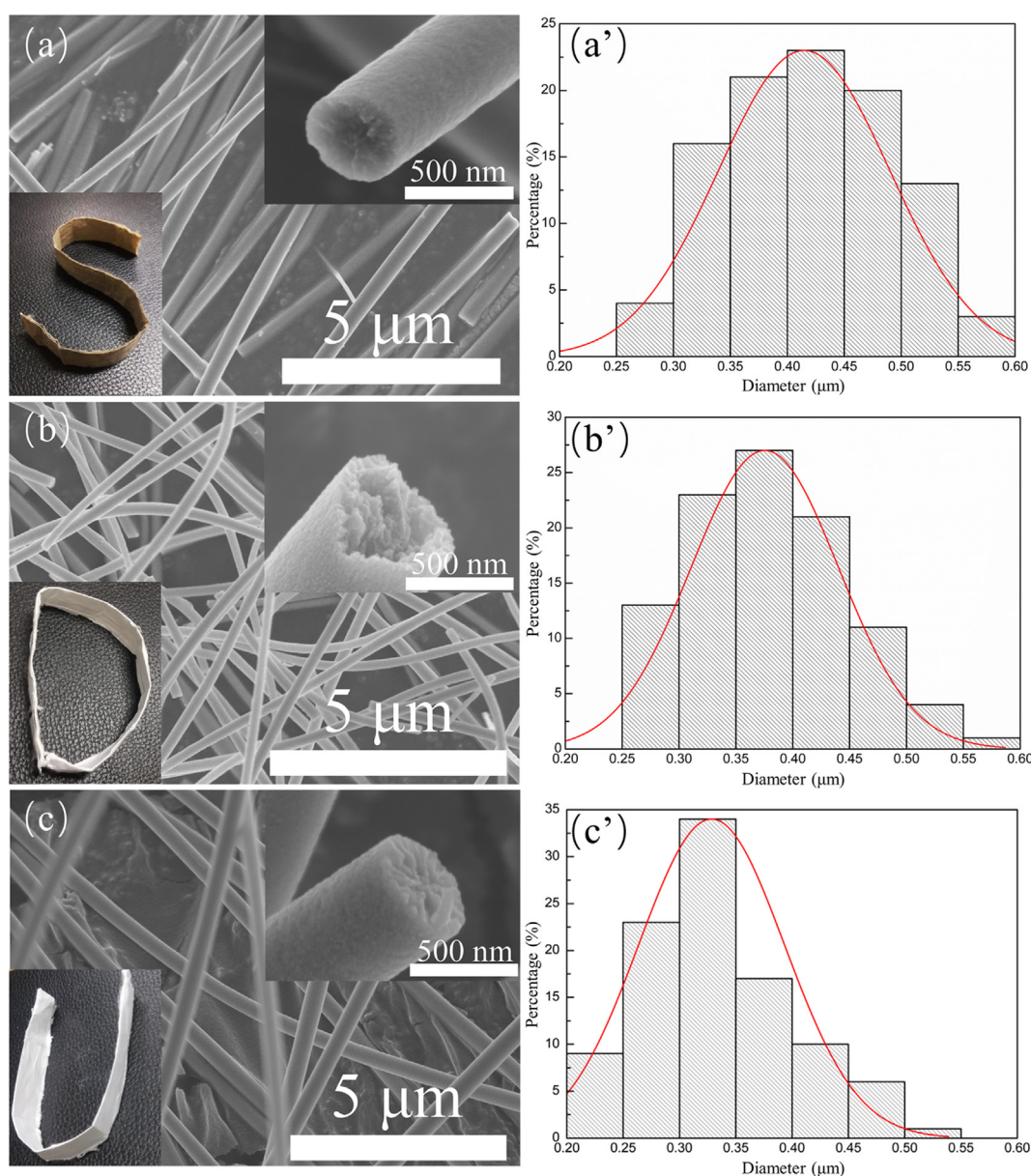


**Fig. 5.** SEM images and diameter distribution chart of samples with the  $\text{Y}_2\text{O}_3$  precursor nanofiber treated at 600 °C, 700 °C and 800 °C for 2 h. The illustrations show cross-sections and optical photographs of nanofibers.

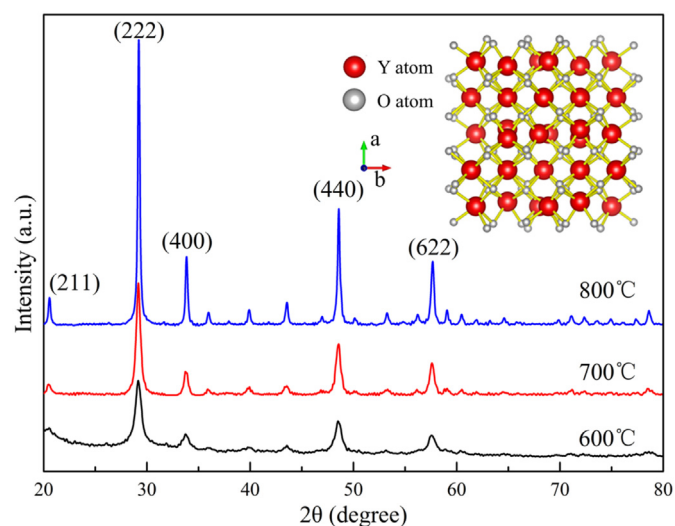


Fig. 6. XRD patterns of yttrium oxide nanofibers at different processing temperatures. The illustration presents a  $\text{Y}_2\text{O}_3$  cell simulation.

ethanol solution were significantly larger than the particles in sample C. This finding was attributed to the tendency of Y–OH interaction in samples A and B to form a three-dimensional structure with abundant Y (OH)<sub>3</sub>. Large particles could hinder filtration. Triethylamine hydrochloride was not easily removed, hence the increased amount of residual triethylamine hydrochloride in samples A and B. In sample C, the linear structure was formed by the interaction of Y–OH. The sample consisted of smaller particles in the solution, which facilitated filtering. The residual amount of triethylamine hydrochloride in sample C was considerably smaller than those in samples A and B. Meanwhile, the D and E solutions showed reduced concentrations because of the removal of precipitates generated by the reaction, and the solubility of

triethylamine hydrochloride in the solution was increased, thereby increasing the triethylamine hydrochloride content in samples D and E.

The  $^1\text{H}$  NMR spectra of precursors A to E and the attribution of each peak are shown in Fig. 3. The integral area of partial chemical shift peaks and their relationships are listed in Table 1. The peaks of d and e are attributed to triethylamine hydrochloride on the basis of the integral area (The integral area ratio of d to e is about 1.5, as shown in Table 1), displacement, and splitting multiplicity. The reason is that the triphenylamine hydrochloride was not completely removed from the product. The content of residual triethylamine hydrochloride was identified with the FT-IR result. Table 1 shows that the integral area ratio of f to g is approximately 1:6, which is consistent with the chemical shift peaks of the enol form of acetylacetone marked in Fig. 3. Acetylacetone as a  $\beta$ -diketone, its enol form is easily coordinated with metal ions, and no chemical shift peak of the hydroxy was found in the enol form of acetylacetone. This finding indicated that enol-like acetylacetone (–acac) coordinated with Y ion. FT-IR analysis indicated the presence of Y–OH is present in the samples. The chemical shift peak j was derived from Y–OH. Only –acac and hydroxyl groups (–OH) could coordinate with Y ion. Thus, the amount of Y–acac in the precursor could be estimated from the integral area ratio of j to f (denoted by j/f). The tendency was that the smaller the value of j/f, the greater the Y–acac content. Table 1 shows that, the value of j/f from samples A to E decreases from 2.70 to 0.78. This reduction is attributed to the stronger ability of the acetylacetonate group to coordinate with the metal ion than that of the hydroxyl group. Therefore, as the molar ratio of acetylacetone to  $\text{YCl}_3 \cdot 6\text{H}_2\text{O}$  increased, the Y–acac content in the samples gradually increased. Increased Y–acac content was detrimental to the spinnable structure formed by Y–OH interaction, leading to a decline in precursor spinning performance, as well as non-spinning performance.

The TG curves of the precursors A to E and the precipitation of ratio E ( $E^*$ ) are shown in Fig. 4. At 800 °C, the remaining amounts of samples A, B, C, D, E, and  $E^*$  were 48%, 49%, 42%, 34%, 30%, and 32%, respectively. The numerical values were considerably larger than the previously reported result [26–29]. The residue of sample A was similar to that of sample B, which might be caused by incomplete drying or impurities (such as triethylamine hydrochloride). With an increase in the molar ratio of acetylacetone to  $\text{YCl}_3 \cdot 6\text{H}_2\text{O}$ , the residual quantity gradually decreased from samples B to E. This finding was attributed to the increase in organic content in the sample resulting from an increase in the molar ratio of acetylacetone to  $\text{YCl}_3 \cdot 6\text{H}_2\text{O}$ . This result is consistent with  $^1\text{H}$  NMR and elemental analysis (Table S2). Sample  $E^*$  still showed 32% mass remaining at 800 °C, which could indicate that the precipitate contained more Y and wasted Y. In addition, the aforementioned result indicated that the Y content in D and E was lower than that in other samples. Thus, they could not be used to prepare precursor nanofibers.

Table 2 shows the spinning performance of samples A, B, and C. First, the stability of the spinning solution prepared using samples A, B and C samples (marked as solutions A, B, and C) was investigated. After allowing the spinning solutions to stand at room temperature for 1 week, a large amount of white precipitate was found in Solution A, whereas a small amount of white precipitate was observed in Solution B. This difference was attributed to the larger amount of Y–OH in Solutions A and B, which led to the further aggregation of a three-dimensional structure formed by Y–OH interaction. Further agglomeration to form large particles produced a precipitate in the solution. However, Solution C remained transparent because of the appropriate Y–OH content in Solution C, and the linear aggregate formed by Y–OH interaction. The linear aggregate could not easily form large particles, and the Solution C was highly stable. Subsequently, the spinning properties of Solutions A, B, and C were evaluated. Precursor nanofibers spun with Solution A were considerably short, only 2–3 cm, and the length of precursor nanofibers spun from Solution B was about 5–7 cm. Most precursor nanofibers spun in Solution C could exceed 10 cm. This finding is attributed to the larger number of three-dimensional aggregation structures found in Solutions A and B, which impeded spinning.

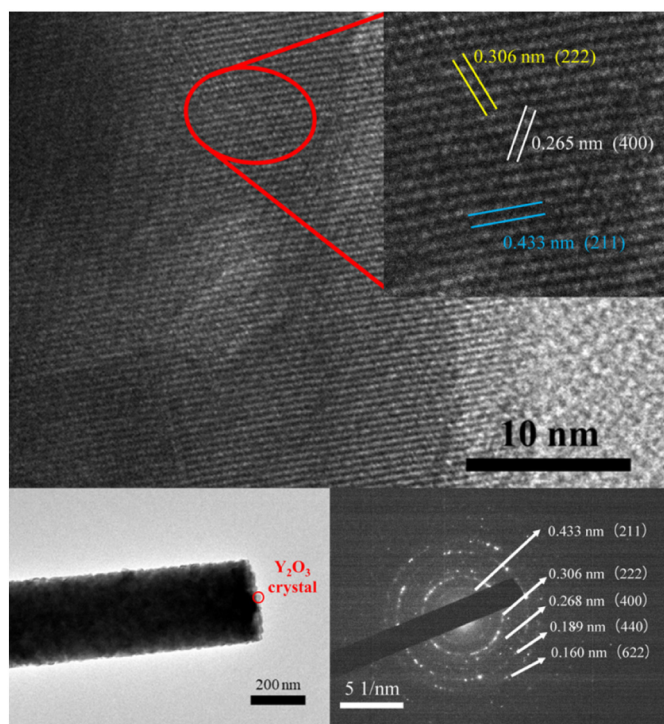


Fig. 7. TEM and HRTEM images (a, b) and SAED pattern (c) of  $\text{Y}_2\text{O}_3$  nanofibers heat-treated at 800 °C.



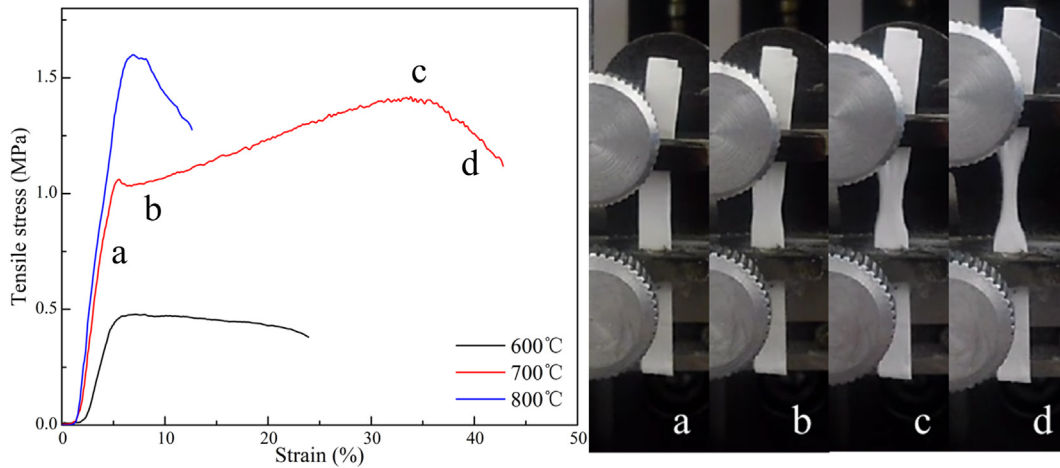


Fig. 8. Stress-strain curves of  $\text{Y}_2\text{O}_3$  nanofiber membrane at 600 °C, 700 °C and 800 °C.

On the basis of the aforementioned, Sample C is an excellent  $\text{Y}_2\text{O}_3$  nanofiber precursor, referred to as PAY.

### 3.2. Crystallization and microstructure

$\text{Y}_2\text{O}_3$  nanofibers were prepared using PAY as a precursor by Electrospinning. SEM was used to characterize the morphological structures and diameters of  $\text{Y}_2\text{O}_3$  nanofibers, and the results are shown in Fig. 5. All nanofibers heat-treated at different temperatures maintained an intact fiber texture morphology. Fig. 5a–c show that the  $\text{Y}_2\text{O}_3$  nanofibers present a continuous morphology. In addition, the figures exhibit the cross-sections and optical photographs of the  $\text{Y}_2\text{O}_3$  nanofiber membrane heat-treated at different temperatures. The nanofibers showed a smooth, dense surface at 600 °C, and no pores or micro-cracks were observed. With an increase in heat treatment temperature, the grain size gradually increased, and the surface became rough with grain growth. The nanofibers had a circular cross-section and the tight arrangement of the grains was clearly visible at the cross-section. The optical photographs that the nanofiber membrane heat-treated at different temperatures revealed multilayer structures with a smooth surface and complete macroscopic morphology. The optical images of the nanofiber membrane clearly show that the  $\text{Y}_2\text{O}_3$  nanofiber membrane could be arbitrarily bent into various shapes, which is significant for its practical

use. Meanwhile, this observation also indicated that the nanofiber membrane exhibited good flexibility and high strength. The strength of the nanofiber membrane is analyzed in subsequent sections. Charts of the diameter distribution of the sample at different temperatures are reflected in Fig. 5a'–c'. The diameter distribution of the fibers was relatively uniform, and the average diameters of the samples obtained at 600 °C, 700 °C, and 800 °C were about 415, 375, and 330 nm, respectively. As heat treatment temperature increased, the diameter of the nanofibers gradually decreased, which was attributed to an increase in crystallinity leading to a decrease in internal defects and an increase in density.

The XRD patterns in Fig. 6 show that all diffraction peaks can be indexed to the cubic  $\text{Y}_2\text{O}_3$  (JCPDS 79-1257) and no peak from any other phase of  $\text{Y}_2\text{O}_3$  and impurities is observed, indicating that the product is single-phase sample. As the heat treatment temperature increased, the intensity of the diffraction peaks increased. The peaks became sharpened, indicating an increase in crystallinity. The grain size and crystallinity of the nanofibers were calculated using Jade 6.0. Both grain size and crystallinity increased with the heat treatment temperature. The crystallinity of the nanofiber increased from about 90% at 600 °C to about 100% at 800 °C. This increase suggested that the crystal grains inside the nanofiber continuously developed and grew up during heating. During this process, the density of the nanofibers increased, whereas the diameter decreased. When the sample was heat-treated at 800 °C, grain size was about 35 nm, which was the same size as that observed in the SEM image (Fig. 5c).

The HRTEM image of  $\text{Y}_2\text{O}_3$  nanofibers heat-treated at 800 °C is presented in Fig. 7a. Lattice fringes and the well crystallized nanofibers are observed. Clear crystal lattice stripes show lattice distance of 0.433, 0.306 and 0.265 nm corresponding to the (211), (222) and (400) lattice planes of cubic phase  $\text{Y}_2\text{O}_3$  (JCPDS 79-1257), respectively. Fig. 7b presents the TEM image of the  $\text{Y}_2\text{O}_3$  nanofiber heat-treated at 800 °C. Similar to the SEM image (Fig. 5c), the TEM image shows the complete morphology of the nanofiber. Crystal grains are clearly observed on the surface and cross-section of the nanofiber, appearing relatively uniform in size and densely arranged. The SAED pattern of the nanofiber (Fig. 7c) was presented at least five diffraction rings, which match the (211), (222), (400), (440) and (622) lattice plane of the cubic phase  $\text{Y}_2\text{O}_3$ .

### 3.3. Mechanical properties of $\text{Y}_2\text{O}_3$ nanofiber membrane

The quality of the mechanical properties is important for the practical use of the flexible nanofiber membrane. However, no studies on the tensile strength of the  $\text{Y}_2\text{O}_3$  nanofiber membrane have been reported. To evaluate the mechanical properties of the  $\text{Y}_2\text{O}_3$  nanofiber membrane, tensile strength tests were conducted. The stress-strain curves of the

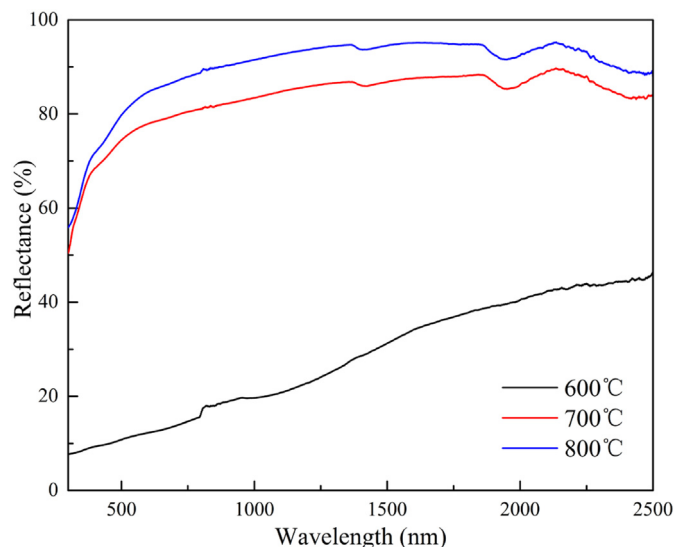


Fig. 9. DRS curves of a  $\text{Y}_2\text{O}_3$  nanofiber membrane heat-treated at different temperatures.

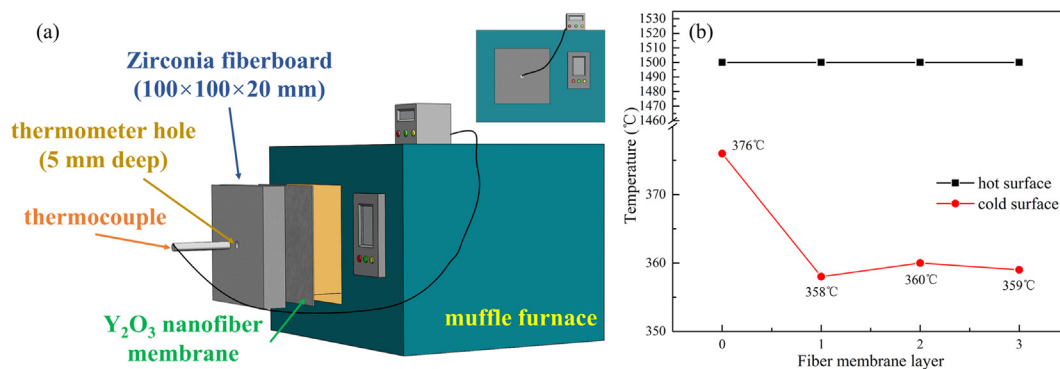


Fig. 10. The schematic diagram of the test device (a) and the hot and cold surface temperature after inserting different layers of  $\text{Y}_2\text{O}_3$  nanofiber membranes on the hot surface (b).

samples heat-treated at different temperatures are presented in Fig. 8. With an increase in heat treatment temperature, the tensile strength of the nanofiber membrane gradually increased. The reason is that as the heat treatment temperature increased, the degree of densification of the nanofiber gradually increased and defects within the nanofibers gradually decreased. The tensile strength of the samples heat-treated at 800 °C could reach 1.6 MPa. Notably, the stress-strain curves of the nanofiber membranes heat-treated at different temperatures varied. The sample treated at 700 °C exhibited high strength, and the nanofiber membrane was gradually tightened from its loose state during stretching (stage a). When the tensile stress exceeded the maximum static friction between nanofibers, the nanofibers slide relative to each other, and the strain gradually increased (stage b). Owing to the roughness of the nanofiber in the surface, the sliding friction force was higher, and the relative slip between nanofibers was difficult. With an increase in the strain during the drawing process, “necking” occurred in the nanofiber membrane, similar to that observed in metal rod during stretching (stage c). The stress in the curve increased slightly. When the contact between the nanofibers was reduced, the stress gradually decreased, eventually reaching the breaking threshold (80% of the maximum stress); the system then defaulted to the nanofiber membrane breaks (stage d). Similarly, owing to the low strength of the sample treated at 600 °C, relative slipping of the nanofibers occurred immediately after straining. The nanofibers had a smooth surface, facilitating the relative slip-page between the nanofibers; no “neck shrinkage” was observed in the nanofiber membrane. As the nanofiber membrane gradually lengthened, contact between the nanofibers gradually decreased, which led to a slight reduction in stress until the fracture threshold was reached. The strength of the sample heat-treated at 800 °C was high and stress increased during tensioning. When the stress reached the maximum static friction force between nanofibers, it gradually decreased and the sample entered the relative sliding stage. However, the friction between the nanofibers was lower than the fracture threshold. The strength tester defaults that the nanofiber membrane was breakage at this stage. In addition, factors such as the diameter of the fiber and the orientation of nanofibers in the nanofiber membrane, affect tensile strength, which will be analyzed in future studies.

#### 3.4. NIR reflective and high-temperature heat-reflecting properties

Fig. 9 shows the reflectance of a  $\text{Y}_2\text{O}_3$  nanofiber membrane as a function of the wavelength between 300 and 2500 nm. The average reflectance of the samples heat-treated at 600 °C–800 °C were about 28%, 83%, and 90%. The reflectivity of the samples at 700 °C and 800 °C were considerably higher than that at 600 °C, which could be attributed to the absorption of a greater amount of infrared light by the sample heat-treated at 600 °C (brown in color). The average reflectivity of the sample heat-treated at 800 °C exceeded 92% in the NIR band

(wavelength range of 750–2500 nm), and the maximum could reach 95%. This value was larger than that of  $\text{Y}_2\text{O}_3$  nanospheres prepared at the same heat treatment temperature, 90% [18]. The reflectivity of the sample heat-treated at 800 °C was greater than that at 700 °C, which was attributed to the increased crystallinity of the  $\text{Y}_2\text{O}_3$  nanofibers at 800 °C.

Diffuse reflectance analysis indicated the high reflectance of the  $\text{Y}_2\text{O}_3$  nanofiber membrane. Reflectance was higher at 750–2500 nm. According to Wien’s displacement law,  $\lambda = b/T$ , where  $b = 2.8977729 (17) \times 10^{-3} \text{ m} \cdot \text{K}$ . The corresponding blackbody radiation temperature is about 885 °C–3590 °C. For single crystals and glass with relatively transparent radiation, radiative heat transfer clearly occurs at 773 K–1273 K, and radiative heat transfer of translucent or opaque oxide refractories clearly occurs at high temperatures of 1773 K [34]. The thermal reflection performance of the  $\text{Y}_2\text{O}_3$  nanofiber membrane was evaluated at 1500 °C in this experiment. The schematic of the test device is presented in Fig. 10a. A self-made zirconia fiberboard (size  $100 \times 100 \times 20 \text{ mm}$ , density  $0.5 \text{ g/cm}^3$ ) was plugged into a muffle furnace door at 1500 °C. The measured stable temperature of the cold surface was 376 °C. Then, different layers of  $\text{Y}_2\text{O}_3$  nanofiber membranes (thickness of about 100  $\mu\text{m}$ ) stacked together was applied to the side of the fiberboard near the furnace cavity, the stable temperature of the cold surface was showed in Fig. 10b. It could clearly show that there was almost no change in the cold surface temperature,  $359 \pm 1$  °C, after inserting different layers of  $\text{Y}_2\text{O}_3$  nanofiber membranes on the hot side. This proved that the role of the  $\text{Y}_2\text{O}_3$  nanofiber membranes were mainly to reflect the heat radiation.

#### 4. Conclusions

For the purpose of high-quality yttrium oxide nanofibers membrane, in the present research, electron-spinnable polyacetylacetone-yttrium precursor was achieved firstly via the optimized coordination reaction between acetylactone and  $\text{YCl}_3 \cdot 6\text{H}_2\text{O}$ . The as-obtained yttrium precursor with the best spinnability, which the molar ratio of -acac to yttrium was 1:1, was considered to origin from the optimized molecular structure, in which the  $\text{Yacac}(\text{OH})_2$  monomer clustered though the interaction of hydroxyl groups. In addition, the  $\text{Y}_2\text{O}_3$  content in the precursor was reached up to as high as 42%, promising the high mechanical strength of the yttrium oxide nanofibers membrane after heat treatment. Secondly, flexible, high crystalline cubic  $\text{Y}_2\text{O}_3$  nanofiber membranes with uniform diameters of about 330 nm were successfully obtained through electronspun the optimal precursor into precursor fiber membrane followed by heat treatment at 800 °C. What’s more, the tensile strength of the as-obtained  $\text{Y}_2\text{O}_3$  nanofiber membrane was as high as 1.6 MPa. The high strength  $\text{Y}_2\text{O}_3$  nanofiber membrane has excellent NIR reflectivity, and the highest value could reach up to 95%. Most importantly, the  $\text{Y}_2\text{O}_3$  nanofiber membrane has a certain shielding effect on the NIR radiation which generated by high temperature. With a hot surface temperature of 1500 °C and using a zirconia fiber sheet as a

heat insulating material, the temperature of the cold surface can be reduced by about 20 °C after adding a layer of Y<sub>2</sub>O<sub>3</sub> nanofiber membrane with a thickness of about 100 μm on the hot surface. It is expected to serve as a reflective screen for high-temperature insulation materials, and to produce multilayer insulation materials which could be used continuously in oxidizing environments combination with high-temperature refractory materials.

## Acknowledgements

The authors thank the National Natural Science Foundation of China, China (Grant Nos. 51472144 and 51372140), Shandong University Young Scholars Program, China (2016WLJH27), Shandong Provincial Natural Science Foundation of China (ZR2017BEM009) and Youth Science Funds of Shandong Academy of Sciences, China (2018QN0031).

## Author contribution

The manuscript was written through contributions of all authors. The author order is consistent with its contribution to the manuscript. All authors have given approval to the final version of the manuscript.

## Notes

The authors declare no competing financial interest.

## Appendix A. Supplementary data

The following files are available free of charge.

Photograph of the solution A, B, C, D, and E; particle size distribution of solution A, B, and C; the results of the elemental analysis of samples A, B, and C (PDF).

Video of the fiber membrane stretching process (MP4). Supplementary data to this article can be found online at <https://doi.org/10.1016/j.matdes.2018.10.017>.

## References

- [1] L. Boltzmann, Ueber eine von Hm. Bartoli entdeckte Beziehung der Wärmestrahlung zum zweiten Hauptsatz, *Ann. Phys. (Berlin)* 258 (1884) 31–39.
- [2] M. Spinnler, E. R.F. Winter, R. Viskanta, T. Sattelmayer, Theoretical studies of high-temperature multilayer thermal insulations using radiation scaling, *J. Quant. Spectrosc. Ra. Transfer* 84 (2004) 477–491.
- [3] Y. Li, S. Mei, Y. Byon, J. Wang, G. Zhang, Highly solar radiation reflective Cr<sub>2</sub>O<sub>3</sub>-3TiO<sub>2</sub> orange nanopigment prepared by a polymer-pyrolysis method, *ACS Sustain. Chem. Eng.* 2 (2014) 318–321.
- [4] Y. Zhai, Y. Ma, S.N. David, D. Zhao, R. Lou, G. Tan, R. Yang, X. Yin, Scalable-manufactured randomized glass-polymer hybrid metamaterial for daytime radiative cooling, *Science* 355 (2017) 1062–1066.
- [5] K. Daryabeigi, Thermal analysis and design optimization of multilayer insulation for reentry aerodynamic heating, *J. Spacecr. Rocket* 39 (2002) 509–514.
- [6] J.E. Fesmire, W.L. Johnson, Cylindrical cryogenic calorimeter testing of six types of multilayer insulation systems, *Cryogenics* 89 (2018) 58–75.
- [7] J.A. Paivanas, *Insulation Construction*, US Patents 1965.
- [8] D. Matsuura, Red, green, and blue upconversion luminescence of trivalent-rare-earth ion-doped Y<sub>2</sub>O<sub>3</sub> nanocrystals, *Appl. Phys. Lett.* 81 (2002) 4526–4528.
- [9] A.O.G. Dikovska, P.A. Atanasov, M.J.D. Castro, A. Perea, J. Gonzalo, C.N. Afonso, J.G. Lopez, Optically active Er<sup>3+</sup>-Yb<sup>3+</sup> codoped Y<sub>2</sub>O<sub>3</sub> films produced by pulsed laser deposition, *Thin Solid Films* 500 (2006) 336–340.
- [10] M.B. Korzenski, P. Lecoer, B. Mercey, D. Chippaux, B. Raveau, R. Desfeux, PLD-grown Y<sub>2</sub>O<sub>3</sub> thin films from Y metal: an advantageous alternative to films deposited from yttria, *Chem. Mater.* 12 (2000) 3139–3150.
- [11] S. Zeng, K. Tang, T. Li, Z. Liang, 3D flower-like Y<sub>2</sub>O<sub>3</sub>: Eu<sup>3+</sup> nanostructures: template-free synthesis and its luminescence properties, *J. Colloid Interface Sci.* 316 (2007) 921–929.
- [12] A. Stupakiewicz, K. Szerenos, D. Afanasiev, A. Kirilyuk, A.V. Kime, Ultrafast nonthermal photo-magnetic recording in a transparent medium, *Nature* 542 (2017) 71–74E.
- [13] L. Wang, H. Huang, X. Ren, J. Wang, D. Shen, Y. Zhao, W. Zhou, P. Liu, D. Tang, Nano-second pulse generation at 2.7 μm from a passively Q-switched Er:Y<sub>2</sub>O<sub>3</sub> ceramic laser, *IEEE J. Sel. Top. Quant.* 24 (2018) 1–6.
- [14] Z. Zhu, D. Gao, G. Yang, J. Zhang, J. Zhang, Z. Shi, F. Xu, H. Gao, D. Xue, Room temperature ferromagnetism in pure Y<sub>2</sub>O<sub>3</sub> nanoparticles, *Europhys. Lett.* 97 (2012), 17005.
- [15] J. Zhang, Z. Hao, J. Li, X. Zhang, Y. Luo, G. Pan, Observation of efficient population of the red-emitting state from the green state by non-multiphonon relaxation in the Er<sup>3+</sup>-Yb<sup>3+</sup> system, *Light-Sci. Appl.* 4 (2015) e239.
- [16] R.J. Cava, B. Batlogg, R.B. Vandover, D.W. Murphy, S. Sunshine, T. Siegrist, J.P. Remeika, E.A. Rietman, S. Zahurak, G.P. Espinosa, Bulk superconductivity at 91K in single-phase oxygen-deficient perovskite Ba<sub>2</sub>YCu<sub>3</sub>O<sub>9-δ</sub>, *Phys. Rev. Lett.* 58 (1987) 1676–1679.
- [17] A.W. Sleight, Chemistry of high-temperature superconductors, *Science* 242 (1988) 1519–1527.
- [18] J. Liu, H. Lv, Z. Wang, F. Wang, H. Luo, X. Yu, Correlations between shape and near infrared reflective properties of nano/micro-Yttria, *J. Nanosci. Nanotechnol.* 11 (2011) 3616–3620.
- [19] A. Konrad, T. Fries, A. Gahn, F. Kummer, U. Herr, R. Tidecks, K. Samwer, Chemical vapor synthesis and luminescence properties of nanocrystalline cubic Y<sub>2</sub>O<sub>3</sub>: Eu, *J. Appl. Phys.* 86 (1999) 3129–3133.
- [20] M. Hajizadeh-Oghaz, R.S. Razavi, M. Barekat, M. Naderi, S. Malekzadeh, M. Rezaadeh, Synthesis and characterization of Y<sub>2</sub>O<sub>3</sub> nanoparticles by sol-gel process for transparent ceramics applications, *J. Sol-Gel Sci. Technol.* 78 (2016) 682–691.
- [21] Z. Jiang, L. Zhang, Q. Yao, S. Wei, T. Zhou, Y. Ben, R. Sun, G. Huang, H. Chen, Y. Wang, Agitator dependent homogeneity enhancement of co-precipitation reaction for improving the dispersibility of precursors and Y<sub>2</sub>O<sub>3</sub> powders, *Ceram. Int.* 43 (2017) 16121–16127.
- [22] A. Paulraj, P. Natarajan, K. Munnisamy, M.K. Nagoor, K.P. Nattar, B. Abdulrazak, J. Duraisamy, Photoluminescence efficiencies of nanocrystalline versus bulk Y<sub>2</sub>O<sub>3</sub>: Eu phosphor-revisited, *J. Am. Ceram. Soc.* 94 (2011) 1627–1633.
- [23] X. Bai, H. Song, L. Yu, L. Yang, Z. Liu, G. Pan, S. Lu, X. Ren, Y. Lei, L. Fan, Luminescent properties of pure cubic phase Y<sub>2</sub>O<sub>3</sub>/Eu<sup>3+</sup> nanotubes/nanowires prepared by a hydrothermal method, *J. Phys. Chem. B* 109 (2005) 15236–15242.
- [24] Y.G. Kim, H.S. Kimb, S.M. Jo, S.Y. Kim, B.J. Yang, J. Chob, S. Leea, J.E. Chab, Thermally insulating, fire-retardant, smokeless and flexible polyvinylidene fluoride nanofibers filled with silica aerogels, *Chem. Eng. J.* 351 (2018) 473–481.
- [25] H. Ji, R. Zhao, N. Zhang, C. Jin, X. Lu, C. Wang, Lightweight and flexible electrospun polymer nanofiber/metal nanoparticle hybrid membrane for high - performance electromagnetic interference shielding, *NPG Asia Mater.* (2018)<https://doi.org/10.1038/s41427-018-0070-1>.
- [26] H. Yu, H. Song, G. Pan, S. Li, Z. Liu, X. Bai, T. Wang, S. Lu, H. Zhao, Preparation and luminescent properties of europium-doped yttria fibers by electrospinning, *J. Lumin.* 124 (2007) 39–44.
- [27] M.M. Munir, K.M. Yun, F. Iskandar, A. Yabuki, K. Okuyama, Heating profile effect on morphology, crystallinity, and photoluminescent properties of Y<sub>2</sub>O<sub>3</sub>: Eu<sup>3+</sup> phosphor nanofibers prepared using an electrospinning method, *Jpn. J. Appl. Phys. Part 1* 46 (2007) 6705–6709.
- [28] G. Dong, Y. Chi, X. Xiao, X. Liu, B. Qian, Z. Ma, E. Wu, H. Zeng, D. Chen, J. Qiu, Fabrication and optical properties of Y<sub>2</sub>O<sub>3</sub>: Eu<sup>3+</sup> nanofibers prepared by electrospinning, *Opt. Express* 17 (2009) 22514–22519.
- [29] X. Li, Y. Chen, Q. Qian, X. Liu, L. Xiao, Q. Chen, Preparation and photoluminescence characteristics of Tb-, Sm- and Dy-doped Y<sub>2</sub>O<sub>3</sub> nanofibers by electrospinning, *J. Lumin.* 132 (2012) 81–85.
- [30] M. Jung, J. Tao, W.M. Kriven, J. Schneider, Preparation and characterization of praseodymium calcium manganate, *Mater. Chem. Phys.* 78 (2003) 778–784.
- [31] K. Yuan, Z. Yu, C. Xu, C. Feng, X. Gan, X. Wang, L. Zhu, G. Zhang, D. Xu, Fabrication of dense barium zirconate fibers by electrospinning with different complex agents, *J. Am. Ceram. Soc.* 100 (2017) 4491–4499.
- [32] M. Aghazadeh, A.A.M. Barmi, H.M. Shiri, S. Sedaghat, Cathodic electrodeposition of Y(OH)<sub>3</sub> and Y<sub>2</sub>O<sub>3</sub> nanostructures from chloride bath. Part II: effect of the bath temperature on the crystal structure, composition and morphology, *Ceram. Int.* 39 (2013) 1045–1055.
- [33] C. Han, Y. Ma, C. Pei, Preparation and characterization of silica composite xerogels with broadband absorption in mid- and far-infrared windows broadband absorption in mid- and far-infrared windows, *J. Non-Cryst. Solids* 369 (2013) 5–10.
- [34] Z. Guan, T. Zhang, J. Jiao, *Physical Properties of Inorganic Materials*, 1st ed. Tsinghua University Press, Beijing, 1992.